

Hybrid Active Modulation Strategy for Three-Level Neutral-Point-Clamped Converters in High-Speed Aerospace Drives

Feng Guo, *Member, IEEE*, Tao Yang, *Senior Member, IEEE*, Ahmed M. Diab, *Student Member, IEEE*, Zhen Huang, *Member, IEEE*, Seang Shen Yeoh, Serhiy Bozhko, *Senior Member, IEEE*, and Patrick Wheeler, *Fellow, IEEE*

Abstract—In the aircraft electric starter/generator (ESG) system, the three-level neutral-point-clamped (3L-NPC) converters play a crucial role in driving turbofan engines and delivering onboard electrical power. However, the conventional pulse-width-modulation (PWM) strategies face the challenge of capacitor voltage deviation, large common-mode voltage (CMV) and extra switching losses. Regarding the characteristics of the studied wide-speed range aerospace drives, the modulation scheme needs to be designed according to its operating conditions. To tackle the above demerits, a hybrid active modulation (HYAM) approach is hence proposed in this paper. By the coordinate-based PWM, the nearest-three-vector is used in the startup process as the neutral-point (NP) voltage balance can be realized with fewer switching intervals; when the drives run in generation mode, an enhanced carrier-based virtual-space-vector modulation technique is involved, which aims to eliminate NP voltage fluctuation, suppress common-mode voltage (CMV) and simplify the modulation process. With the help of bias-offset injection in the time and voltage domain, capacitor voltages can be effectively kept at a balanced state even though the imbalance exists. The validity of the presented algorithm is proved by simulation and experimental results obtained from a 45 kW, 32 krpm aircraft starter/generator test rig.

Index Terms—Common-mode voltage (CMV), capacitor voltage balance, coordinate-based hybrid modulation, more-electric-aircraft (MEA), three-level topology.

I. INTRODUCTION

THE more-electric-aircraft (MEA) concept has received much attention in the development of next-generation large, commercial aircraft due to its high reliability, low maintenance costs and good environmental impact [1]–[3]. To fulfill these expectations, aerospace systems are undergoing a transition from pneumatic, hydraulic and mechanical power to

This work was supported by the Clean Sky 2 Joint Undertaking under Grant 807081. (*Corresponding author: Zhen Huang.*)

F. Guo is with the Power Electronic System Laboratory at Arkansas (PESLA), Department of Electrical Engineering, University of Arkansas, Fayetteville, AR 72701, USA (email: fengg@uark.edu)

A. M. Diab is with the Key Laboratory of More Electric Aircraft Technology of Zhejiang Province, University of Nottingham Ningbo China, Ningbo, China (e-mail: ahmed.diab@nottingham.edu.cn)

Z. Huang is with School of Information Engineering, Nanchang University, Nanchang, China. (email: zhenhuang@ncu.edu.cn).

T. Yang, S. S. Yeoh, S. Bozhko and P. Wheeler are with the Power Electronics, Machines and Control (PEMC) Group, the Department of Electrical and Electronic Engineering, The University of Nottingham, Nottingham NG7 2RD, U.K. (email: tao.yang@nottingham.ac.uk; serhiy.bozhko@nottingham.ac.uk; pat.wheeler@nottingham.ac.uk)

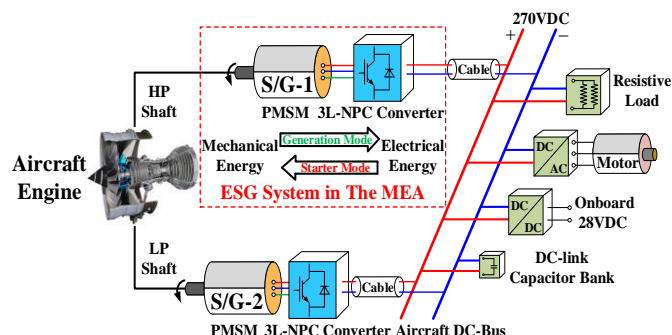


Fig. 1. Configuration of the studied ESG system in the MEA.

electrical counterparts [4], [5]. Thanks to the cutting-edge active rectification technology [6], an advanced aircraft electric starter/generator (ESG) system tends to substitute the typical three-stage wound-field synchronous generator for avoiding mechanical failures, especially for high-speed operation (over 20 krpm). Fig.1 shows the structure of the ESG system that is mainly composed of a high-speed motor and an active front end (AFE), where two sets of starter/generator (S/G) take power from the main engine through high pressure (HP) shaft and low pressure (LP) shaft, as referred to [7], and operate in parallel to transfer the power to the aircraft DC bus. Because of lower blocking voltage across semiconductors, and smaller filter size, the three-level neutral-point-clamped (3L-NPC) converter is selected as an energy conversion kit [8], [9].

To be more specific, the PMSM is mechanically coupled to the aircraft engine shaft and is electrically connected with a 3L-NPC converter that interfaces the S/G and onboard electric power system (EPS) accordingly [6]. During the engine startup process, the converter-fed motor drives are used to crank and accelerate aircraft engine. Then, engine ignition is triggered when machine speed raises to 10 krpm. After that, the ESG system is in standby mode. In order to enable the PMSM to operate in the high-speed region, deep flux-weakening currents are injected, which results in the power factor gradually descending from 0.7 to 0.2. Once the motor speed approaches 20 krpm, the generation mode activates and the modulation index is up to 0.9 [10]. In this mode, the engine cranks the high-speed machine that runs as an electric generator, while the 3L-NPC converter works as a rectifier to convert this variable frequency AC into DC bus and to supply aircraft EPS.

Nevertheless, a major problem with this kind of topology is the NP voltage imbalance even though the natural balancing method [11] and the self-balancing effect [12] sometimes work. Over-stress voltage caused by capacitor voltage deviation may

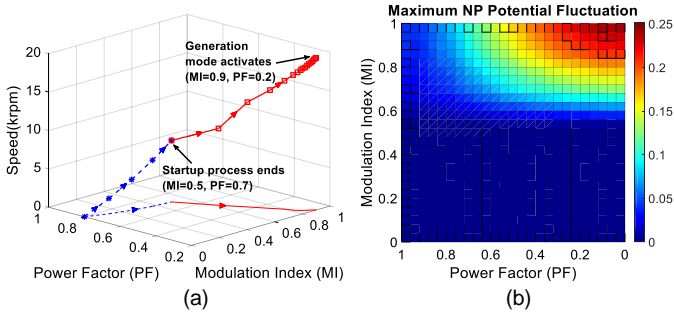


Fig. 4. The characteristics for wide-speed range operation of the ESG system (a) Correlation among modulation index, power factor and speed during a T_{ESG} . (b) Normalized amplitude of NP voltage fluctuation.

TABLE I
SWITCHING PRINCIPLE OF 3L-NPC CONVERTER

Switching State	Switch Status				Output Voltage Level
	VT_{x1}	VT_{x2}	VT_{x3}	VT_{x4}	
P	1	1	0	0	$V_{dc}/2$
O	0	1	1	0	0
N	0	0	1	1	$-V_{dc}/2$

the CBPWM with optimal switching states-based [31], [34]. So far, however, there has been little discussion about the hybrid PMM scheme from the coordinate-based perspective.

To this end, this paper proposes a novel hybrid active modulation (HYAM) technique that bridges the gap between hybrid PWM and two-dimensional variables for the 3L-NPC converter-fed high-speed aerospace motor drives. Based on the operating characteristics of the developed ESG system, the PWM modulator deploys the g - h coordinate-based NTVs in a low modulation index region that corresponds to the startup process. Therefore, the unnecessary switching action can be avoided, as opposed to the NTV² scheme. As the voltage stress on its winding would be substantially increased if the CMV is imposed on machine terminals, and also its steep changes can induce damaging ground leakage, bearing currents and emission of common-mode noise, a superior VSV-based PWM strategy with suppressed CMV is employed in generation mode so that the reliability can be improved. In addition, the modulation waves that are projected to the reference space vector's position in a form of g - h coordinates aim to simplify the modulation process and offer more degrees of freedom. To recover the drifted capacitor voltages, hybrid bias-offsets are injected in form of time and voltage domains, accordingly.

The rest of this paper is organized as follows. The principles of the aircraft ESG system are briefly introduced in Section II. The proposed HYAM algorithm, along with the simplified dwell time and modulation wave determination approaches, is presented in Section III. The effectiveness of the modulation technique is verified by simulation and experimental results given in Section IV and Section V, respectively. Finally, the main conclusions of this work are summarized in Section VI.

II. PRINCIPLES OF ESG SYSTEM

A. Control Design and Characteristics of ESG System

The ESG system control blocks presented in Fig.3 involve flux-weakening control, machine speed control and DC-link current control. The speed control is activated in starter mode

TABLE II
SPACE VECTORS, SWITCHING STATES AND NP CURRENTS OF 3L-NPC CONVERTER

Space Vectors	Switching States		NP Currents	
Zero Vector	[PPP]	[OOO]	[NNN]	-
Small Vector	P-type		N-type	
	[POO]	[OON]	$-I_a$	I_a
	[PPO]	[OON]	I_c	$-I_c$
	[OPO]	[NON]	$-I_b$	I_b
	[OPP]	[NOO]	I_a	$-I_a$
	[POP]	[ONO]	I_b	$-I_b$
	[OOP]	[NNO]	$-I_c$	I_c
Medium Vector	[PON]		I_b	
	[OPN]		I_a	
	[NPO]		I_c	
	[NOP]		I_b	
	[ONP]		I_a	
Large Vector	[PNO]		I_c	
	[PNP]	[PPN]	[NPN]	-
	[NPP]	[NNP]	[PNP]	

TABLE III
CMV ANALYSIS OF SWITCHING STATE AND SPACE VECTORS

Space Vectors	Switching States	$ V_{cm} $
Zero Vector	[OOO]	0
	[PPP] [NNN]	$V_{dc}/2$
Small Vector	[POO] [OON] [OPO] [NON] [OOP] [ONO]	$V_{dc}/6$
	[ONN] [PPO] [NON] [OPP] [NNO] [POP]	$V_{dc}/3$
Medium Vector	[PON] [OPN] [NPO] [NOP] [ONP] [PNO]	0
Large Vector	[PNN] [PPN] [NPN] [NPP] [NNP] [PNP]	$V_{dc}/6$

and DC-link current is regulated by droop characteristics in generation mode. The vector control technique is used for machine decoupling purposes, which allows controlling flux and torque independently. Hence, machine torque represented as active power is controlled by q -axis current. A large negative d -axis current is needed during the high-speed operation, which results in a lower power factor in the steady-state.

It is notable that the wide-speed range operation of the studied ESG system features variable modulation index and power factor, as shown in Fig.4(a), where the converter serves as an inverter during 20% of a T_{ESG} , and then it will work as a rectifier for the rest of operational time, in which T_{ESG} (typically about 200 seconds) is defined as the time when the aircraft ESG systems launch from the standstill to the speed of 20 krpm.

B. Three-Level Topology and G-H Reference Frame

As shown in Fig.2, each phase-leg composes of four IGBTs ($VT_{x1} \sim VT_{x4}$) and two clamping-diodes (DZ_{x1} and DZ_{x2}), in which $x = \{A, B, C\}$. Two equal capacitors (C_1 and C_2) are series-connected to form the DC-link. For a 3L-NPC converter, 27 switching states can be produced in total. When VT_{x1} and VT_{x2} are turned on, the switching state is denoted as P, and output voltage level is $V_{dc}/2$. The switching state O indicates that VT_{x2} and VT_{x3} are turned on, which produces zero voltage. The switching state N means that VT_{x3} and VT_{x4} are turned on and output voltage is $-V_{dc}/2$. VT_{x1} is complementarily switched with VT_{x3} . VT_{x2} and VT_{x4} also follow the same manner. Table I details the switching principle. The combination of these states can be grouped into zero, small, medium and large vectors, wherein small ones are 12 while the number of large ones and

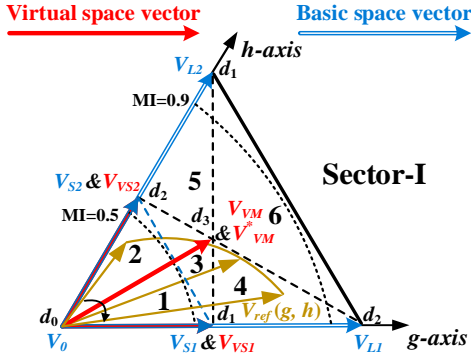


Fig. 5. SVD of the proposed HYAM strategy in Sector-I.

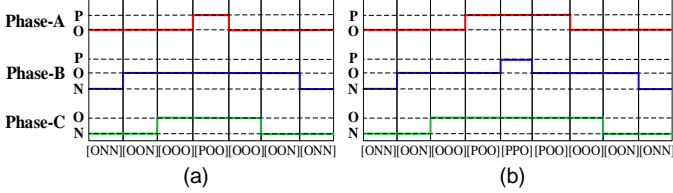
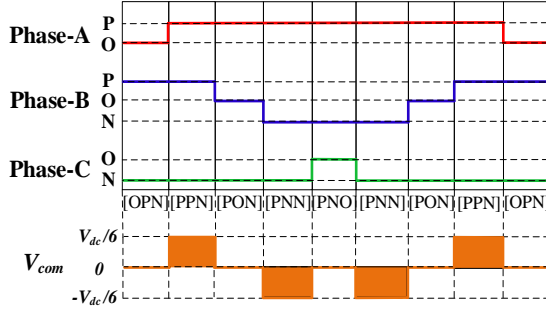

 Fig. 6. Switching pattern comparison during the startup process (a) The proposed HYAM scheme. (b) The original NTV² scheme.


Fig. 7. Pulse train of the proposed strategy for subsector 6 of Sector-I.

medium ones are both 6, and the rest is zero vector.

In order to approximate the reference voltage vector, the dwell time of each vector needs to be calculated. However, the computational effort suffers from cumbersome trigonometric functions for the conventional α - β reference frame [22]. As a result, before presenting the proposed HYAM technique afterward, the g - h reference frame that replaces the orthogonal coordinate system is established via a transformation matrix:

$$\begin{bmatrix} V_g \\ V_h \end{bmatrix} = \begin{bmatrix} 1 & -\frac{1}{\sqrt{3}} \\ 0 & \frac{2}{\sqrt{3}} \end{bmatrix} \begin{bmatrix} V_\alpha \\ V_\beta \end{bmatrix} \quad (1)$$

C. NP Voltage Imbalance and Large CMV Issues

Since the current flowing into and out of the midpoint of DC bus depends on the magnitude and polarity of phase current, as found in Table II, the converter output variables have an impact on the NP potential. For our designed ESG system, the NP voltage drift can be calculated by the work of [22]. The results from Fig.4(b) indicate the ripple is aggravated in the case of unity modulation index and power factor at the vicinity of zero.

In addition, the CMV for a given converter, denoted by V_{com} , is defined by:

$$V_{com} = (V_{ao} + V_{bo} + V_{co}) / 3 \quad (2)$$

where V_{ao} , V_{bo} and V_{co} represents the three-phase pole voltages.

With (2), CMVs are listed in Table III. As can be seen, except [PPP] and [NNN], the maximum magnitude is $V_{dc}/3$. It indicates that both the conventional NTV and NTV² schemes fail to suppress larger CMV components from the source as all small vectors are fully utilized over a fundamental period.

III. PROPOSED HYBRID ACTIVE MODULATION STRATEGY

In the following text, the proposed HYAM technique is presented in each subsection. Without loss of generality, Sector-I is chosen as a representative example to explain.

A. Principle of Hybrid Modulation Strategy

The g - h reference frame based space vector diagram (SVD) of the proposed algorithm is shown in Fig.5. It should be pointed out that the projection of V_{ref} in the new plane is normalized with the magnitude of large space vector ($2/3V_{dc}$). Thus, (g, h) refers to a unique coordinate that can identify each position of space vector inside the hexagon. For example, the coordinate of the medium vector in the first sector is (0.5, 0.5).

According to the sector further partition, when V_{ref} falls into subsector 1, it is synthesized by redundant small vector V_{S1} denoted by [POO] and [ONN], small vector V_{S2} indicated by [OON] and zero vector V_0 represented by [OOO]. The specific switching pattern in the startup process by the proposed HYAM strategy is shown in Fig.6(a). A similar rule applies to subsector 2. In contrast, the original NTV² scheme used in this operating zone involves two VSVs, denoted as V_{VS1} and V_{VS2} in Fig.5, which are synthesized by [POO] and [ONN], [PPO] and [OON] altogether, thus leading to five switching states [21]. Fig.6(b) gives the firing pulses by the NTV² scheme in case the modulation index is below 0.5. As shown, two switching actions have been omitted as compared to the original NTV² scheme applied in the ESG system at this stage. With the modulation index exceeding 0.5, however, the NTV scheme leads to a large NP voltage ripple [20]. Hence, deploying VSVs is preferred in subsectors 3-5 for the purpose of eliminating low-frequency NP voltage fluctuation. More importantly, the VSV that is consisted of two redundant small vectors is suitable for NP current control when an error exists in the NP.

On the other hand, to lower the risk of premature motor bearing failure rendered by shaft current, the basic vectors composing VSV should be chosen based on their CMVs. In our case, more attention needs to be given to subsector 6, this is because most output vectors are near the hexagon side in the system's steady-state. It is known from Tables II-III that not only can the adjacent three medium vectors realize zero CMV but also NP currents are produced in a form of three-phase currents. Given the target drives are three-phase balance, the enhanced virtual medium vector is used to obtain inherent NP voltage balance and CMV mitigation at once, which has been firstly presented in our previous work of [23] and [35]. The specific definition is given by (3). Fig.7 shows the resultant pulse trains by the HYAM strategy for subsector 6 of Sector-I, where CMV has been constrained within $\pm V_{dc}/6$. Besides, compared with the traditional 7-segment pulse pattern, the extra two switching actions displayed in Fig.7 facilitate a trade-off for NP voltage balance and CMV mitigation when the target

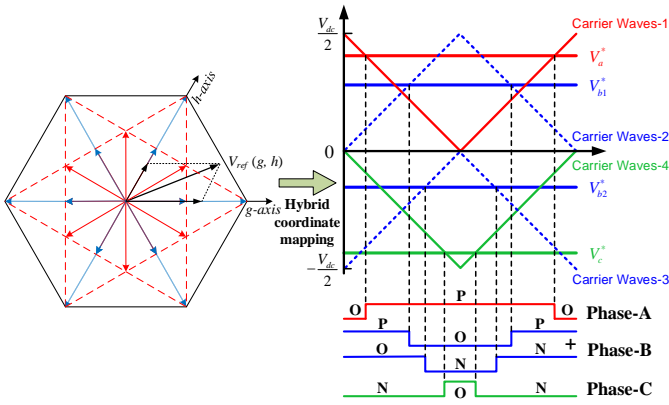


Fig. 8. Carrier-based implementation with coordinate mapping for the proposed HYAM strategy in subsector 6 of Sector-I.

system operates at a high speed in generation mode.

$$\begin{cases} V_{L1} = V_{[PNN]} \\ V_{VM}^* = (V_{[OPN]} + V_{[PON]} + V_{[PNO]})/3 \\ V_{L2} = V_{[PPN]} \end{cases} \quad (3)$$

The core principle of the above space vector synthesis forms the basis of the proposed HYAM technique in this paper.

B. Carrier-Based Implementation

Due to the multi-segment three-level modulation employed in subsectors 3-6, the dwell time determination and switching pattern configurations must be done if the SVM method is deployed. To facilitate algorithmic efficiency further, the generation of the desired pulse trains in these regions can be performed by the carrier-based SVM implementation.

With regard to subsector 6, however, the transition instant of [P]→[O]→[N] in phase-B differs from [O]→[P] and [N]→[O] in the other two phases. In order to realize such a switching sequence, carrier wave-2 and 3 are adopted. V_b^* is decomposed as V_{b1}^* and V_{b2}^* so as to obtain three-level commutations over a carrier period, together with the hybrid coordinate mapping relationship, as shown in Fig.8. Consequently, the specific modulation signals can be derived as follows:

$$\begin{cases} V_a^* = V_{dc} / 2 \cdot (g + h) \\ V_{b1}^* = V_{dc} / 2 \cdot h \\ V_{b2}^* = V_{dc} / 2 \cdot -g \\ V_c^* = V_{dc} / 2 \cdot -(g + h) \end{cases} \quad (5)$$

Through deriving carrier-based VSV modulation waves for subsectors 3-5, the findings show that (5) is the generalized expression for the first sextant. It should be point out that four carrier waves are required to configure in terms of subsector 6. Similar calculations can be also carried out for other sectors. In addition, by (1) and (5), it is noticeable that only one coordinate transformation, i.e., the α - β reference frame to the g - h reference frame, is sufficient to produce three-phase modulation signals.

In addition, it is worth noting that the coordinate-based form for the proposed hybrid PWM exhibits the potential to expand the degree of freedom. This is because, first of all, the method inherits the capability of offset variable injection as same as the conventional CBPWM scheme, such as NP voltage balancing control that will be presented in the next subsection. Secondly,

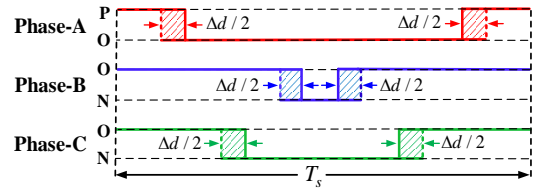


Fig. 9. Capacitor voltage balancing control with the time-domain offset injection in subsector 1.

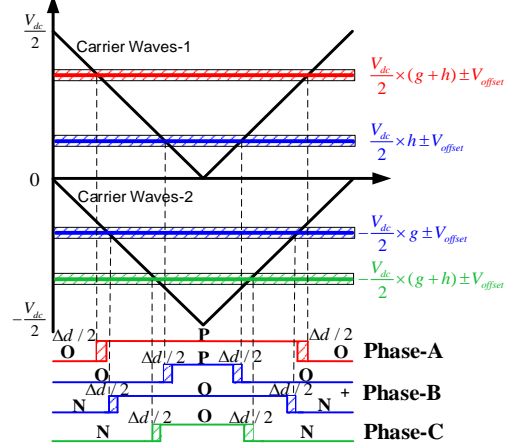


Fig. 10. Capacitor voltage balancing control with voltage-domain offset injection in subsector 4.

as seen from (5), the g - h coordinate provides a decomposition capability in one phase for some specific sectors, leading to the average zero NP current. Most importantly, the third degree of freedom is achieved by means of establishment between two-variable input and desirable modulation signals. For example, the DC-link voltage utilization improvement techniques through special reference voltage vector tracks have been investigated in our works of [24] and [36], which is worth exploring further for this study in the future.

C. Capacitor Voltage Balancing Control

Another key issue that needs to be addressed is capacitor voltage balancing control when NP potential initially shifts. Here, the coefficient k is utilized to measure the imbalance voltage range ΔV_{dc} , as defined by:

$$\begin{cases} k = \frac{V_{dc1}}{V_{dc1} + V_{dc2}} \\ \Delta V_{dc} = (2k - 1)(V_{dc1} + V_{dc2}) \end{cases} \quad (6)$$

where $k \in [0, 1]$, V_{dc1} and V_{dc2} represent the upper and lower-side capacitor voltage, respectively.

From (6), it is clear that NP voltage is balanced if k is 0.5. Otherwise, active balancing control must remove the existing error. The average NP currents is calculated by:

$$\overline{I_{NP}} = \sum_{x=a,b,c} d_{xo} \cdot i_x \quad (7)$$

where d_{xo} represents the duty cycle of switching state O. i_x refers to phase current.

Further, the DC-voltage bias in the NP can be yielded by:

$$\Delta V_{NP} = \frac{1}{C} \int_{t=0}^{t=T_s} \overline{I_{NP}} \cdot dt \quad (8)$$

It implies that the tendency of capacitor voltage divergence is determined by the average current flowing into the NP over a switching cycle. From Table II and (7), it is known that the redundant switching states need a phase duty cycle offset Δd .

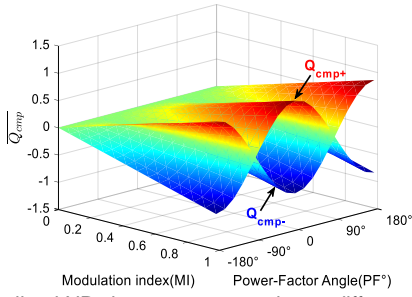


Fig. 11. Normalized NP charge compensation at different MI and PF.

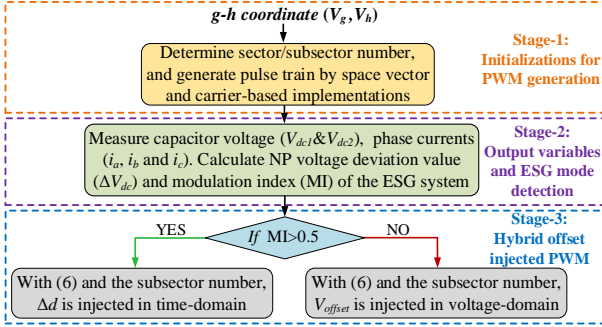


Fig. 12. Flowchart of the NP voltage balancing control algorithm for the proposed HYAM strategy.

Due to the symmetry of subsectors 1-2, the balance control method for subsector 1 is taken as a case study.

Case I: when $k \in [0, 0.5)$. In order to regulate NP potential drift, the dwell time of [ONN] proportionally grows with ΔV_{dc} , whereas the dwell time of [POO] should be dropped down.

As illustrated in Fig.9, phase-A is clamped between positive DC-rail and the NP, whereas phase-B and C are both clamped between the NP and negative DC-rail. Based on corresponding switching pattern and (8), the compensated electric charge can be derived as:

$$C \cdot \Delta V_{dc} = -[(1-g+\Delta d)i_a + (1-g-\Delta d)i_b + (1-g-2h-\Delta d)i_c] \cdot T_s \quad (9)$$

where Δd is the duty cycle offset and T_s is a switching cycle.

Then, Δd can be calculated as:

$$\Delta d = -\left(\frac{C \Delta V_{dc}}{2T_s i_a} + \frac{i_c}{i_a} h\right) \quad (10)$$

Case II: if $k \in (0.5, 1]$, the dwell time of [ONN] needs to be decreased to recover the imbalance, whereas the dwell time of [POO] should be inversely regulated. Thus, Δd is expressed as the opposite sign value of (10).

With the machine speed ramping up and modulation index deepening, the generation mode is enabled. This indicates that subsectors 3-6 will be involved. Fig.10 shows the switching pulses and modulation waves in the case of subsector 4. As can be seen, both phase-A and C generate two consecutive voltage levels as compared to phase-B clamping to the NP and positive/negative rail of DC-link accordingly. For this scenario, two cases are considered as follows:

Case I: if $k \in [0, 0.5)$, to keep the balanced condition, small vector [POO] should become predominant in comparison with [ONN]. The compensated electric charge is calculated by:

$$C \cdot \Delta V_{dc} = -[(1-g-h-\Delta d)i_a + (1-g-h-\Delta d+\Delta d)i_b + (1-g-h+\Delta d)i_c] \cdot T_s \quad (11)$$

Further, Δd and the corresponding offset in voltage-domain

can be derived as:

$$\begin{cases} \Delta d = \frac{C \Delta V_{dc}}{2T_s (i_a - i_c)} \\ V_{offset} = \Delta d \cdot \frac{V_{dc}}{2} \end{cases} \quad (12)$$

Case II: if $k \in (0.5, 1]$, the dwell time of [POO] needs to be declined to raise the NP potential. Meanwhile, the switching instant of [ONN] becomes wider in this situation. Similarly, Δd is obtained as the opposite sign value of (12).

Due to the unavailability of small vectors in subsector 6, the provided method can hardly correct the diverged NP voltage in that region. This is a trade-off for suppressing CMV. In spite of that, the reference voltage vector can still pass through subsectors 4-5, where redundant switching states are ready to be tailored, to maintain NP voltage balanced when the target system runs in the case of a modulation index of 0.9. Moreover, this simple control design benefits computational efficiency.

As seen from (10) and (12), the compensation capability is determined by NP currents that vary at different modulation indices and power factor angles. Consequently, the average compensated NP electric charge over a fundamental cycle is adopted to evaluate the capability of the proposed active NP voltage balancing control method. Here, subsector-4 of the first sector is taken as an example to explain. The average amount of compensated electric charge can be calculated as:

$$\begin{aligned} \overline{Q_{cmp}} &= \frac{1}{2\pi} \int_{t=0}^{t=2\pi} Q_{cmp}(\omega t) \cdot dt \\ &= \frac{1}{2\pi} \int_{t=0}^{t=2\pi} (1-2k)(1-g-h)(i_a - i_c) \cdot dt \\ &= \frac{(1-2k)}{2\pi} \int_{t=0}^{t=2\pi} [1 - m \sin(\frac{\pi}{3} - \omega t) - m \sin(\omega t)] \\ &\quad \cdot [\cos(\omega t - \varphi) - \cos(\omega t + \frac{2\pi}{3} - \varphi)] \cdot dt \end{aligned} \quad (25)$$

where ω is the angular frequency, m refers to the modulation index and φ represents the power factor angle.

By using a similar derivation for other subsectors over a fundamental period, the dedicated electric charge is plotted in Fig.11. As shown, Q_{cmp+} and Q_{cmp-} can be effectively generated by the provided approach. Furthermore, the amount increases along with the deepening modulation index. Although the maximum compensation is achieved under unity power factor condition, the state of NP potential can be kept balanced during the entire operating points of the studied ESG system.

Fig.12 displays the three-stage implementation starting from a simple $g-h$ coordinate to produce hybrid pulse trains with active capacitor voltage balancing control.

IV. SIMULATION RESULTS

A simulation model for the aircraft ESG system is built in the Simulink/PLECS environment and its parameters are listed in Table IV. In order to demonstrate the NP voltage balance, CMV and power losses of the proposed HYAM strategy, the conventional NTV and NTV² schemes are chosen as the benchmark method in the following. The operating conditions with two modulation indices and power factors are carried out in the simulations, which refer to the motoring and generation

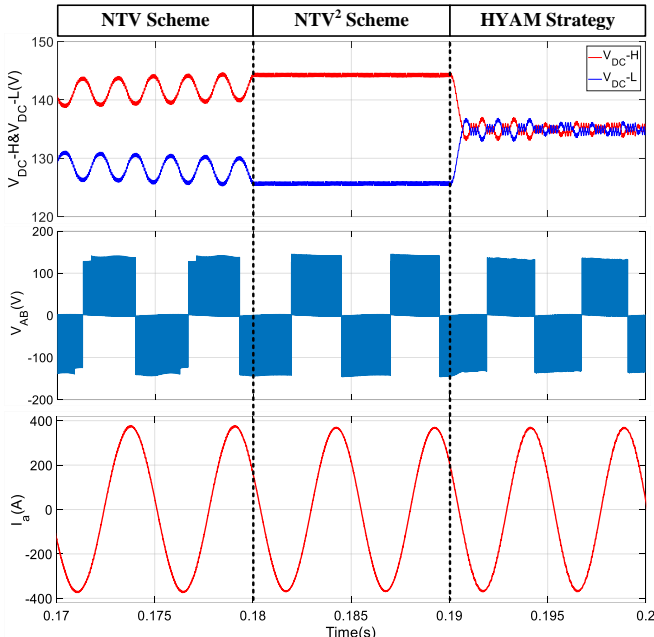


Fig. 13. Simulation results in starter mode (MI=0.5 and PF=0.7).

mode of the converter-fed drive systems, respectively.

A. Capacitor Voltage Balancing Capability

Fig.13 shows that, during the startup process, two shifted capacitor voltages under the benchmark method are converged when switching to the presented modulation strategy. In addition, less distortion in line-to-line voltage indicates better performance in the lower modulation index region. Regarding generation mode, the proposed HYAM technique realizes balanced NP voltage compared with its counterparts, as illustrated in Fig.14. More importantly, the capacitor voltage fluctuation is greatly eliminated even though the ESG system operates in a modulation index of 0.9 and power factor of 0.2. It should be noted that, as the result of applied non-nearest space vectors, the output current harmonic distortion is unavoidably aggravated, which facilitates a trade-off for CMV suppression. Moreover, this issue will become less outstanding for power converters with a short switching period.

B. CMV Suppression Performance

The CMV in the ESG system in the steady-state is given in Fig.15. As shown, the main component of CMVs caused by the NTV and NTV² schemes are $\pm V_{dc}/3$. In this regard, however, the proposed method primarily produces CMV of $\pm V_{dc}/6$.

C. Power Loss Analysis

The semiconductor loss analysis is performed by the applied Infineon F3L400R07ME4_B22/B23 insulated-gate bipolar transistor (IGBT) module. The switching frequency is set at 16 kHz, DC-link voltage is 270V and the power rating is 45 kW. By using characteristic curves in the manufacturer's datasheet, the power loss is calculated by the PLECS simulation tools.

Fig.16 presents the comparison of power loss distribution based on the conventional NTV, NTV² scheme, and the proposed solution at a modulation index of 0.5 and 0.9 under a power factor of 0.7 and 0.2. It can be seen that the total amount of loss by the proposed strategy is the same as that of the NTV scheme in starter mode. Since the HYAM strategy also induces

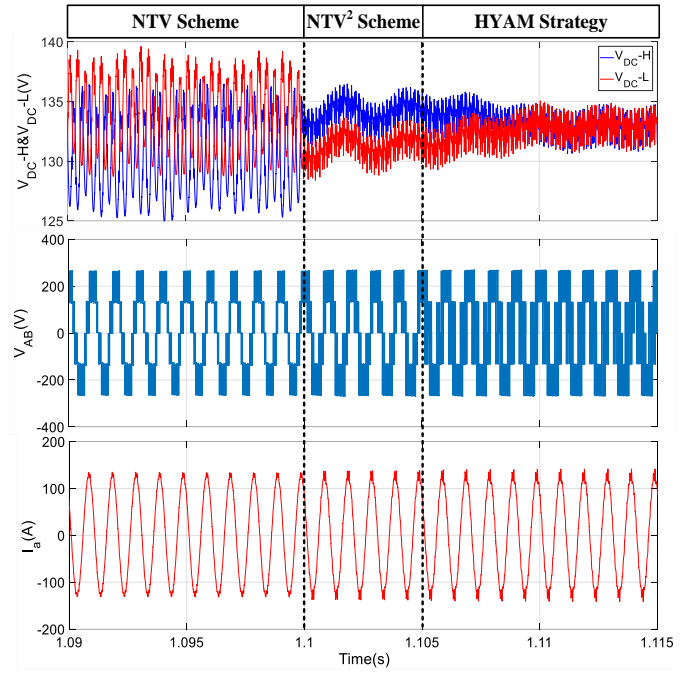


Fig. 14. Simulation results in generation mode (MI=0.9 and PF=0.2).

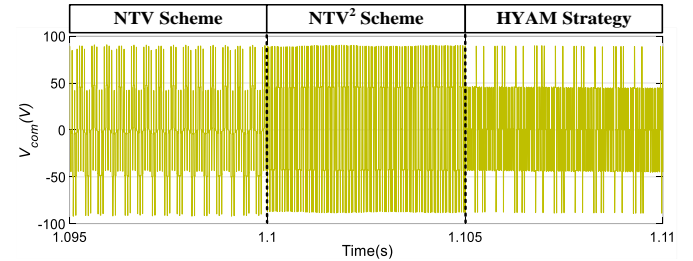


Fig. 15. CMV of the ESG system under the NTV, NTV² scheme and the proposed HYAM strategy in generation mode.

three-level transitions under power generation conditions, as illustrated in Fig.7 and Fig.14, the switching losses are thus similar to that of the NTV² scheme at the steady stage.

D. Comparison With Other Hybrid Modulation Strategies

In comparison with other hybrid PWM strategies for multilevel NPC converters, the proposed modulation technique embraces the following advantages:

- 1) Unlike [29] and [30], with the help of algebraic functions, the duty cycle determination process is simplified to avoid the heavy computational burden.
- 2) By using the provided bias-offset injection method, the NP voltage drift is easily resolved instead of calculating complex analytical solutions of NP currents [32].
- 3) As the switching states are optimally configured, CMVs generated by the proposed method can be substantially suppressed in the steady-state of the systems. However, the main component of that value is at least doubled by the existing hybrid modulation schemes in [28]-[32].
- 4) Though extra switching actions are required compared with the amount in [28], [31] and [34], NP voltage ripple in generation mode is validly eliminated by this work.
- 5) While the hybrid PWM pattern presented in [33] considered the voltage stress and the commutation number, the g - h coordinate-based solution is more

TABLE IV
ESG SYSTEM PARAMETERS

Parameters	Value
$L_d = L_q$	99 μ H
Pole pair	3
Switching/Carrier frequency	16 kHz
PM flux	0.03644 V \cdot rad
Base speed	8000 rpm
Fundamental frequency in generation mode	1~1.6 kHz
Capacitor value ($C_1=C_2$)	600 μ F
DC-link voltage	270 V

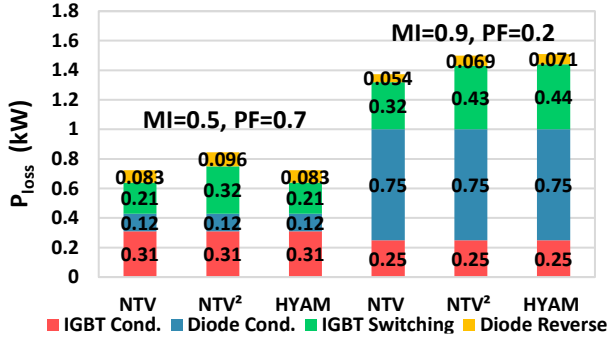


Fig. 16. Comparison of power loss distribution under the conventional NTV, NTV² scheme and the proposed HYAM strategy.

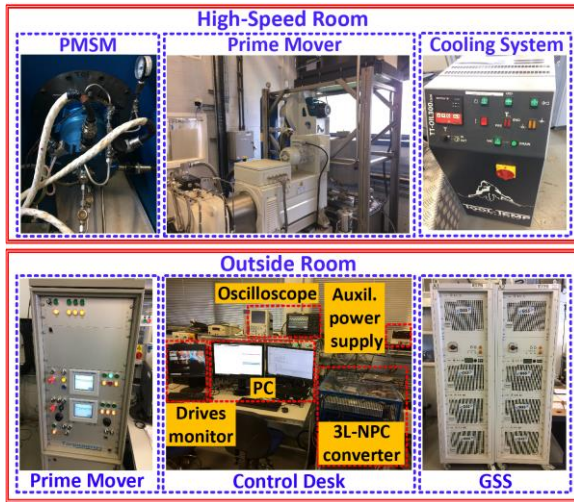
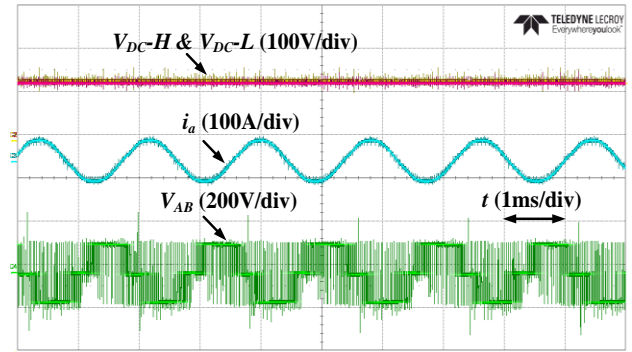


Fig. 17. ESG prototype system test rig.

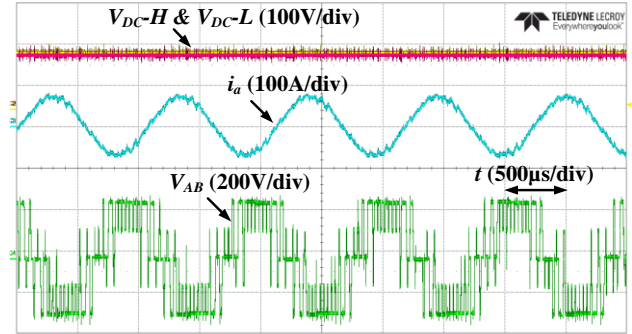
simple and flexible than the traditional implementation in the $a-b-c$ reference frame [33]. Only one coordinate transformation and two independent variables are enough to generate all desired pulse trains.

V. EXPERIMENTAL RESULTS

The proposed HYAM technique is experimentally verified by a 45 kW, 32 krpm ESG prototype system, as shown in Fig.17. A 150 kW prime mover mechanically emulates aircraft engine shaft and is coupled with an oil-cooled PMSM, which are both located in an isolated room for safety consideration. The 3L-NPC converter along with a digital control platform, prime mover controller, host PC and DC source is placed outside the high-speed room. The control platform includes a TMS320C6713 DSP Starter Kit (DSK) and an FPGA-ProAsic3 A3P400 card. PPA5530 is used as a precision power analyzer for monitoring AC-side parameters. The DC bus of the

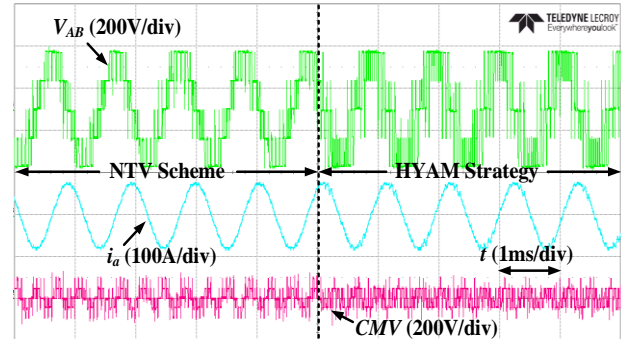


(a)

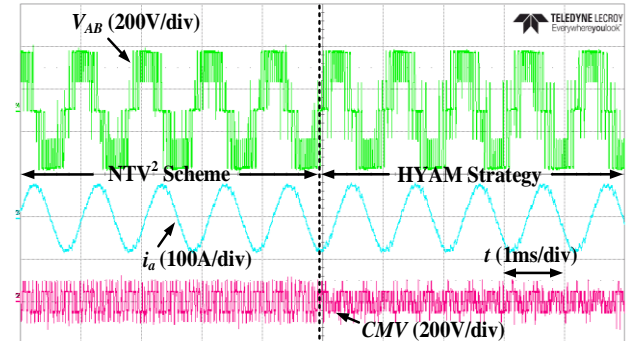


(b)

Fig. 18. The experimental results of the proposed HYAM strategy under (a) The startup process (b) The generation mode.



(a)



(b)

Fig. 19. CMV comparison between the proposed HYAM strategy and (a) The NTV scheme (b) The NTV² scheme.

converter is connected to a grid-tied source-sink (GSS) that mimics onboard 270VDC of the aircraft EPS.

The experimentation of the NTV, NTV² and the proposed HYAM strategy are all performed in the period of starter and power generation mode. The machine rotation speed of 8 krpm,

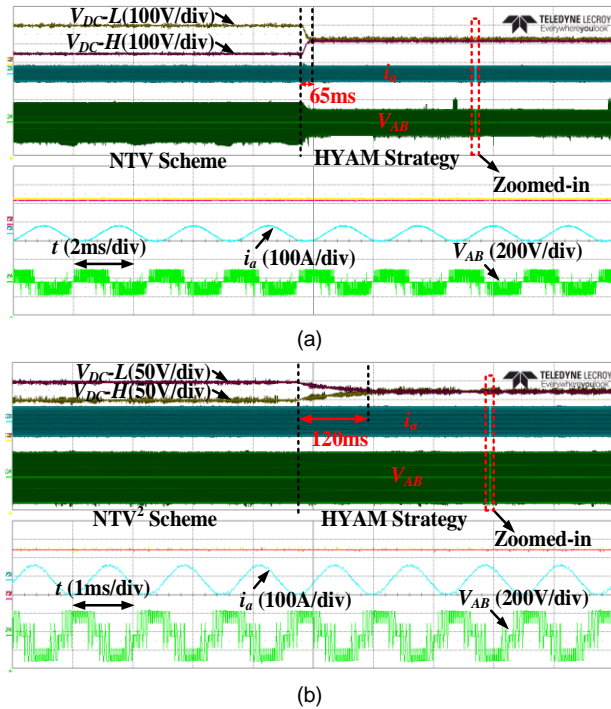


Fig. 20. NP voltage balancing of the proposed HYAM strategy under (a) The startup process (b) The power generation mode.

modulation index of 0.5 and power factor of 0.7 are chosen as a representative operating point of the former occasion, whereas the latter one corresponds to the machine speed of 20 krpm, modulation index of 0.9 and power factor of 0.2. In addition, the steady-state validation primarily focuses on the ESG system operating in light-load conditions as the rapid-changing phase current impairs capacitor voltage balance.

A. Modulation Performance Over A Wide-Speed Range

Fig.18(a) shows two capacitor voltages (V_{DC-H}/V_{DC-L}), line current and phase voltage in the startup process, while Fig.18(b) gives the converter’s output variables in generation mode when delivering 6 kW active power. The results present the well-balanced NP voltage at the above operating points.

The CMV suppression performance is tested by the benchmark method and the proposed HYAM strategy under power generating conditions. As seen from Fig.19(a), the main component of CMVs produced by the provided approach is much lower than that by the NTV scheme. Moreover, the CMVs containing $\pm V_{dc}/3$ are significantly reduced when the PWM modulator switches from the NTV² scheme to the proposed HYAM strategy, as shown in Fig.19(b).

B. Capacitor Voltage Balancing Performance

In order to verify the NP voltage balancing control of the HYAM strategy. Firstly, the above modulation schemes are tested in the startup process with a fundamental frequency of 400 Hz, where NP voltage shifts 70V under the NTV scheme, and the line-to-line voltage is heavily distorted, as shown in Fig.20(a). Nevertheless, the zoomed-in waveform demonstrates that two capacitor voltages can be kept balanced again by the presented algorithm within 65ms. Along with the PMSM speed ramping up, the ESG system runs in generation mode with a fundamental frequency of 1 kHz and an active power of 5 kW,

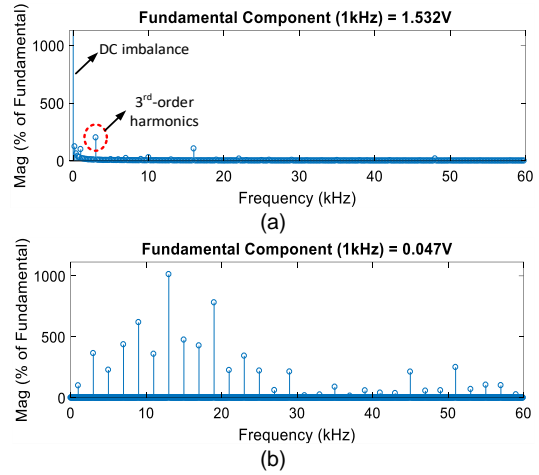


Fig. 21 FFT analysis of NP voltage fluctuation under (a) The NTV scheme (b) The proposed HYAM strategy.

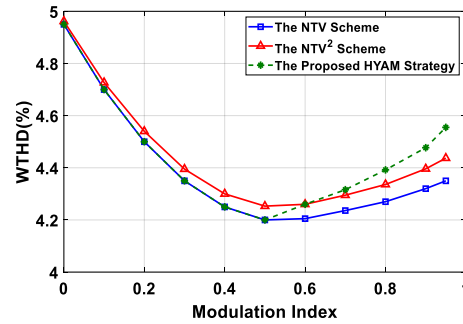


Fig. 22. WHTD of the line-to-line voltage under the NTV, NTV² schemes, and the proposed HYAM strategy at different modulation indices.

similar experimentation is carried out under the NTV² scheme. The experimental results from Fig.20(b) show that NP voltage fails to maintain balance, in which an imbalance voltage of 50V exists. By contrast, output phase voltage is constantly clamped at three levels, the DC-voltage bias in the NP is removed and phase voltage distortion problem is well resolved when the proposed modulation technique is adopted within 120ms.

C. Distortion Analysis

Using FFT analysis on NP potential, its harmonic content can be gained under the traditional seven-segment method and the proposed HYAM strategy, as shown in Fig. 21. It is evident from the results that not only the imbalance issue is tackled by the presented strategy but also the low-frequency NP voltage ripple is greatly eliminated, particularly for 3rd-order harmonics. Fig.22 shows the weighted THD (WTHD) comparison of the line-to-line voltage under the NTV, NTV² and the proposed HYAM strategy at different modulation indices. As shown, the WTHD of the presented technique overlaps with that of NTV when modulation index is lower than 0.5, whereas that value of the NTV² scheme is higher during this period. After that, due to additional three-level switching instants, the distortion of the presented solution arises in the high output voltage region, and induces a higher WTHD, as opposed to the benchmark method.

D. Computational Performance

The computational time for the proposed HYAM strategy is measured by the used microcontroller. The results show that it costs 58.6 μ s to execute the proposed algorithm. In comparison to the traditional implementation method with 68.2 μ s, the computation resources are approximately saved by 16.3%.

VI. CONCLUSION

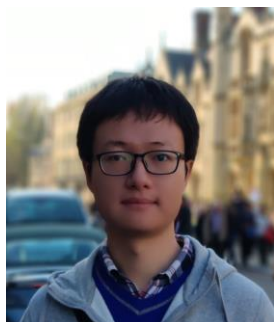
In this paper, a new coordinate-based hybrid PWM strategy has been proposed to enable the high-performance operation of 3L-NPC converter-fed high-speed motor drives in the MEA. With the presented technique, the main contributions of this work lie in: 1) Due to the non-NP-voltage-divergence-prone region in the startup process of the aircraft ESG system, the deployed NTVs achieve capacitor voltage balance easily with fewer switching actions. 2) The enhanced VSV-based PWM scheme enabling low-frequency NP potential ripple elimination and higher components of the CMV suppression is seamlessly supplemented in power generation mode. 3) To pursuit the algorithmic efficiency and flexibility, the equivalence between the hybrid SVM and the g - h coordinate-based CBPWM is revealed. 4) With the independent time and voltage-domain offset control, the presented scheme corrects shifted NP voltage, particularly for high modulation index and low power factor operating conditions. The proposed modulation concept and method can also apply to all 3L-NPC converter-fed variable-speed drive systems. Simulation and experimental results proved the good overall performance of the introduced strategy in terms of capacitor voltage balance, CMVs, power losses, line-to-line voltage and execution time.

More importantly, the hybrid PWM technique is beneficial for selecting proper tracks of reference voltage vector, thereby leading to an additional degree of freedom. In our future work, the extended operating points of the target system will be incorporated in this developed hybrid active modulation algorithm. By doing so, with the DC-link voltage utilization improvement, more advantages would be expected to realize during the cruise stage, such as enhanced output torque capability and reduced flux-weakening current, etc.

REFERENCES

- [1] P. Wheeler, T. S. Sirimanna, S. Bozhko and K. S. Haran, "Electric/hybrid-electric aircraft propulsion systems," *Proc. IEEE*, vol. 109, no. 6, pp. 1115-1127, Jun. 2021.
- [2] G. Buticchi, S. Bozhko, M. Liserre, P. Wheeler and K. Al-Haddad, "On-board microgrids for the more electric aircraft—technology review," *IEEE Trans. Ind. Electron.*, vol. 66, no. 7, pp. 5588-5599, Jul. 2019.
- [3] B. Sarlioglu and C. T. Morris, "More electric aircraft: review, challenges, and opportunities for commercial transport aircraft," *IEEE Trans. Transport. Electrification*, vol. 1, no. 1, pp. 54-64, Jun. 2015.
- [4] C. Jiang and H. Liu, "A novel interleaved parallel bidirectional dual-active-bridge DC-DC converter with coupled inductor for more-electric aircraft," *IEEE Trans. Ind. Electron.*, vol. 68, no. 2, pp. 1759-1768, Feb. 2021.
- [5] J. Yang *et al.*, "Modeling and stability enhancement of a permanent magnet synchronous generator based DC system for more electric aircraft," *IEEE Trans. Ind. Electron.*, doi: 10.1109/TIE.2021.3066934
- [6] S. Bozhko *et al.*, "Development of aircraft electric starter-generator system based on active rectification technology," *IEEE Trans. Transport. Electrification*, vol. 4, no. 4, pp. 985-996, Dec. 2018.
- [7] I. Moir and A. Seabridge, "Aircraft systems: mechanical, electrical and avionics subsystems integration," *John Wiley & Sons*, 2008.
- [8] M. Schweizer, T. Friedli and J. W. Kolar, "Comparative evaluation of advanced three-phase three-level inverter/converter topologies against two-level systems," *IEEE Trans. Ind. Electron.*, vol. 60, no. 12, pp. 5515-5527, Dec. 2013.
- [9] Z. Wang, Y. Wu, M. H. Mahmud, Z. Zhao, Y. Zhao and H. A. Mantooth, "Design and validation of a 250-kW all-silicon carbide high-density three-level T-type inverter," *IEEE J. Emerg. Sel. Topics Power Electron.*, vol. 8, no. 1, pp. 578-588, Mar. 2020.
- [10] C. Li *et al.*, "A modified neutral point balancing space vector modulation for three-level neutral point clamped converters in high-speed drives," *IEEE Trans. Ind. Electron.*, vol. 66, no. 2, pp. 910-921, Feb. 2019.
- [11] M. Aly, E. M. Ahmed and M. Shoyama, "Modulation method for improving reliability of multilevel T-type inverter in PV systems," *IEEE J. Emerg. Sel. Topics Power Electron.*, vol. 8, no. 2, pp. 1298-1309, Jun. 2020.
- [12] J. Shen, S. Schröder, R. Rösner and S. El-Barbari, "A comprehensive study of neutral-point self-balancing effect in neutral-point-clamped three-level inverters," *IEEE Trans. Power Electron.*, vol. 26, no. 11, pp. 3084-3095, Nov. 2011.
- [13] R. Sommer, A. Mertens, C. Brunotte and G. Trauth, "Medium voltage drive system with NPC three-level inverter using IGBTs," in *Proc. IEEE PWM Medium Voltage Drives Semin.*, May 11, 2000, pp. 3/1-3/5.
- [14] J. Wang, Y. Gao and W. Jiang, "A carrier-based implementation of virtual space vector modulation for neutral-point-clamped three-level inverter," *IEEE Trans. Ind. Electron.*, vol. 64, no. 12, pp. 9580-9586, Dec. 2017.
- [15] S. K. Giri, S. Mukherjee, S. Kundu, S. Banerjee and C. Chakraborty, "An improved PWM Scheme for three-level inverter extending operation into overmodulation region with neutral-point voltage balancing for full power-factor range," *IEEE J. Emerg. Sel. Topics Power Electron.*, vol. 6, no. 3, pp. 1527-1539, Sep. 2018.
- [16] P. Liu, S. Duan, C. Yao and C. Chen, "A double modulation wave CBPWM strategy providing neutral-point voltage oscillation elimination and CMV reduction for three-level NPC inverters," *IEEE Trans. Ind. Electron.*, vol. 65, no. 1, pp. 16-26, Jan. 2018.
- [17] S. Bhattacharya, D. Mascarella and G. Joos, "Space-vector-based generalized discontinuous pulsewidth modulation for three-level inverters operating at lower modulation indices," *IEEE J. Emerg. Sel. Topics Power Electron.*, vol. 5, no. 2, pp. 912-924, Jun. 2017.
- [18] J. Lee, S. Yoo and K. Lee, "Novel discontinuous PWM method of a three-level inverter for neutral-point voltage ripple reduction," *IEEE Trans. Ind. Electron.*, vol. 63, no. 6, pp. 3344-3354, Jun. 2016.
- [19] S. Mukherjee, S. K. Giri and S. Banerjee, "A flexible discontinuous modulation scheme with hybrid capacitor voltage balancing strategy for three-level NPC traction inverter," *IEEE Trans. Ind. Electron.*, vol. 66, no. 5, pp. 3333-3343, May 2019.
- [20] J. Pou, R. Pindado, D. Boroyevich and P. Rodriguez, "Evaluation of the low-frequency neutral-point voltage oscillations in the three-level inverter," *IEEE Trans. Ind. Electron.*, vol. 52, no. 6, pp. 1582-1588, Dec. 2005.
- [21] S. Busquets-Monge, J. Bordonau, D. Boroyevich and S. Somavilla, "The nearest three virtual space vector PWM-a modulation for the comprehensive neutral-point balancing in the three-level NPC inverter," *IEEE Power Electron. Lett.*, vol. 2, no. 1, pp. 11-15, Mar. 2004.
- [22] F. Guo, T. Yang, C. Li, S. Bozhko and P. Wheeler, "Active modulation strategy for capacitor voltage balancing of three-level neutral-point-clamped converters in high-speed drives," *IEEE Trans. Ind. Electron.*, vol. 69, no. 3, pp. 2276-2287, March 2022.
- [23] F. Guo, T. Yang, A. Diab, S. Yeoh, S. Bozhko and P. Wheeler, "An enhanced virtual space vector modulation scheme of three-level NPC converters for more-electric-aircraft applications," *IEEE Trans. Ind. Appl.*, vol. 57, no. 5, pp. 5239-5251, Sept.-Oct. 2021.
- [24] F. Guo *et al.*, "An overmodulation algorithm with neutral-point voltage balancing for three-level converters in high-speed aerospace drives," *IEEE Trans. Power Electron.*, vol. 37, no. 2, pp. 2021-2032, Feb. 2022.
- [25] W. Alhosaini, F. Diao, M. H. Mahmud, Y. Wu and Y. Zhao, "A virtual space vectors based model predictive control for inherent DC link voltage balancing of three-level T-type converters," *IEEE J. Emerg. Sel. Topics Power Electron.*, vol. 9, no. 2, pp. 1751-1764, Apr. 2021.
- [26] L. Guo, N. Jin, C. Gan, L. Xu and Q. Wang, "An improved model predictive control strategy to reduce common-mode voltage for two-level voltage source inverters considering dead-time effects," *IEEE Trans. Ind. Electron.*, vol. 66, no. 5, pp. 3561-3572, May 2019.
- [27] L. Guo, N. Jin, C. Gan and K. Luo, "Hybrid voltage vector preselection-based model predictive control for two-level voltage source inverters to reduce the common-mode voltage," *IEEE Trans. Ind. Electron.*, vol. 67, no. 6, pp. 4680-4691, Jun. 2020.
- [28] J. Zaragoza, J. Pou, S. Ceballos, E. Robles, P. Ibanez and J. L. Villate, "A comprehensive study of a hybrid modulation technique for the neutral-point-clamped converter," *IEEE Trans. Ind. Electron.*, vol. 56, no. 2, pp. 294-304, Feb. 2009.

- [29] W. Jiang, S. Du, L. Chang, Y. Zhang and Q. Zhao, "Hybrid PWM strategy of SVPWM and VSPWM for NPC three-level voltage-source inverter," *IEEE Trans. Power Electron.*, vol. 25, no. 10, pp. 2607-2619, Oct. 2010.
- [30] C. Xia, H. Shao, Y. Zhang and X. He, "Adjustable proportional hybrid SVPWM strategy for neutral-point-clamped three-level inverters," *IEEE Trans. Ind. Electron.*, vol. 60, no. 10, pp. 4234-4242, Oct. 2013.
- [31] A. Choudhury, P. Pillay and S. S. Williamson, "A hybrid PWM-based DC-link voltage balancing algorithm for a three-level NPC DC/AC traction inverter drive," *IEEE J. Emerg. Sel. Topics Power Electron.*, vol. 3, no. 3, pp. 805-816, Sep. 2015.
- [32] N. Beniwal *et al.*, "A dual-mode modulation technique for controlling the average neutral point current in neutral-point-clamped converters," *IEEE Trans. Power Electron.*, vol. 36, no. 5, pp. 6079-6091, May 2021.
- [33] N. -V. Nguyen and M. -V. Doi, "Carrier based PWM control of 3-level NPC inverter with DC neutral point balancing and common mode voltage reduction," *2019 10th International Conference on Power Electronics and ECCE Asia (ICPE 2019 - ECCE Asia)*, Busan, Korea (South), 2019, pp. 1213-1220.
- [34] M. Lak, Y. -T. Tsai, B. -R. Chuang, T. -L. Lee and M. H. Moradi, "A hybrid method to eliminate leakage current and balance neutral point voltage for photovoltaic three-level T-type inverter," *IEEE Trans. Power Electron.*, vol. 36, no. 10, pp. 12070-12089, Oct. 2021.
- [35] F. Guo, T. Yang, S. Bozhko, and P. Wheeler, "A novel virtual space vector modulation scheme for three-level NPC power converter with neutral-point voltage balancing and common-mode voltage reduction for electric starter/generator system in more-electric-aircraft," in *Proc. IEEE Energy Convers. Congr. Expo.*, Sep. 2019, pp. 1852-1858.
- [36] F. Guo, T. Yang, S. S. Yeoh, S. Bozhko, P. Wheeler and A. M. Diab, "A simple PWM strategy for three-level NPC converters in aircraft electric starter/generator system with improved DC-link voltage utilization and reduced common-mode voltage," in *Proc. IEEE Energy Convers. Congr. Expo.*, Oct. 2021, pp. 4854-4858.



Feng Guo (Member) received his B.Eng. from China University of Mining and Technology, Xuzhou, China, in 2014, and received M.S. (Hons.) from Northeastern University, Shenyang, China, in 2017, both in electrical engineering, and the Ph.D. degree at the Power Electronics, Machines and Control (PEMC) Group in electrical and electronics engineering from the University of Nottingham, Nottingham, U.K., in 2021.

Since January 2022, he has been with the Power Electronic Systems Laboratory at Arkansas (PESLA), University of Arkansas, Fayetteville, AR, USA, as a Postdoctoral Fellow. From 2016 to 2017, he was a visiting student with the Chinese University of Hong Kong, Shenzhen, China. His research interests include pulse-width-modulation strategy, high efficiency and high power-density multilevel converters, wide bandgap power device applications, high-speed motor drives and transportation electrification, etc.



Tao Yang (Senior Member) received his MEng Degree from Shanghai Jiao Tong University, China in 2008 and his Ph.D. degree in electrical engineering from the University of Nottingham, UK in 2013.

Since 2013, he has been a Researcher with Power Electronics, Machines and Control Group, University of Nottingham, where he became an

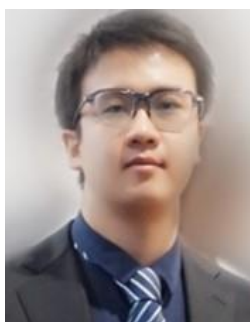
Assistant Professor in 2016, and an Associate Professor in 2019. His research interests include high-speed electric motor drive control, power electronic conversion, electrical system design and optimization for more electric/hybrid/all-electric aircraft applications. His PhD research within EU Clean Sky on "Modelling electrical power system for more-electric aircraft applications" has resulted in him winning the inaugural "Clean Sky Best PhD Award" in 2016.

Dr. Yang is an Associate Editor for the IEEE TRANSACTIONS ON TRANSPORTATION ELECTRIFICATION and Chinese Journal of Aeronautics.



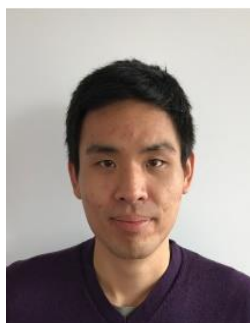
Ahmed M. Diab (Student Member) received the B.Sc. (Hons.) and M.Sc. degrees from Zagazig University, Zagazig, Egypt in 2011 and 2016, respectively. He is currently working toward the Ph.D. degree at the University of Nottingham Ningbo China and Institute for Aerospace technology (IAT), university of Nottingham, Nottingham, UK. From 2011 to 2016, he was a research and

Teaching Assistant with the Department of Electrical Power and Machines, Zagazig University. His research interests include modeling, control, and stability in high-speed motor/generator systems for transportation electrification applications and in variable-speed wind generators.



Zhen Huang (Member) received the B.Eng. degree (Hons.) in electrical and electronics engineering and the Ph.D. degree in electrical engineering from the University of Nottingham, Nottingham, U.K., in 2015 and 2019, respectively.

From January 2020, he was a Research Fellow with the Power Electronics, Machines and Control Group, University of Nottingham. He is currently with the School of Information Engineering, Nanchang University, Nanchang, China. His research interests include high-speed machine drives, multilevel converters, and onboard electrical power system protection for hybrid/all-electric vehicles and more/all-electric aircraft applications.



Seang Shen Yeoh received his MSc degree in power electronics (Distinction) and Ph.D degree in electrical engineering from the University of Nottingham, United Kingdom, in 2011 and 2016 respectively. Since then, he has been a research fellow in the same university under the Power Electronics, Machines, and Controls Research Group. His current

research interests are in the area of aircraft power systems, namely modelling and stability studies of complex power

systems, and new control strategies for high-speed drive systems.



Serhiy Bozhko (Senior Member) received his M.Sc. and Ph.D. degrees in electromechanical systems from the National Technical University of Ukraine, Kyiv City, Ukraine, in 1987 and 1994, respectively. Since 2000, he has been with the Power Electronics, Machines and Controls Research Group of the University of Nottingham, United Kingdom, where

currently he is Professor of Aircraft Electric Power Systems and Director of the Institute for Aerospace Technology. He is leading several EU- and industry funded projects in the area of aircraft electric power systems, including power generation, distribution and conversion, power quality, control and stability issues, power management and optimization, as well as advanced modelling and simulations methods.



Patrick Wheeler (Fellow) received his BEng (Hons.) degree in 1990 from the University of Bristol, UK. He received his PhD degree in Electrical Engineering for his work on Matrix Converters from the University of Bristol, UK in 1994. In 1993 he moved to the University of Nottingham and worked as a research assistant in the Department of

Electrical and Electronic Engineering. In 1996 he became a Lecturer in the Power Electronics, Machines and Control Group at the University of Nottingham, UK. Since January 2008 he has been a Full Professor in the same research group.

He was Head of the Department of Electrical and Electronic Engineering at the University of Nottingham from 2015 to 2018. He is currently the Head of the Power Electronics, Machines and Control Research Group, Global Director of the University of Nottingham's Institute of Aerospace Technology and was the Li Dak Sum Chair Professor in Electrical and Aerospace Engineering. He is a member of the IEEE PELs AdCom and is currently an IEEE PELS Vice-President. He has published over 750 academic publications in leading international conferences and journals.